Random-Phase Approximation Methods

Guo P. Chen, Vamsee K. Voora, Matthew M. Agee, Sree Ganesh Balasubramani, and Filipp Furche

Department of Chemistry, University of California, Irvine, California 92697-2025; email: guo.chen@uci.edu, filipp.furche@uci.edu

Annu. Rev. Phys. Chem. 2017. 68:421–45

First published online as a Review in Advance on March 16, 2017

The *Annual Review of Physical Chemistry* is online at physchem.annualreviews.org

https://doi.org/10.1146/annurev-physchem-040215-112308

Keywords

electronic structure theory, density functional theory, random-phase approximation, electron correlation, small-gap systems, noncovalent interactions

Abstract

Random-phase approximation (RPA) methods are rapidly emerging as cost-effective validation tools for semilocal density functional computations. We present the theoretical background of RPA in an intuitive rather than formal fashion, focusing on the physical picture of screening and simple diagrammatic analysis. A new decomposition of the RPA correlation energy into plasmonic modes leads to an appealing visualization of electron correlation in terms of charge density fluctuations. Recent developments in the areas of beyond-RPA methods, RPA correlation potentials, and efficient algorithms for RPA energy and property calculations are reviewed. The ability of RPA to approximately capture static correlation in molecules is quantified by an analysis of RPA natural occupation numbers. We illustrate the use of RPA methods in applications to small-gap systems such as open-shell *d*- and *f*-element compounds, radicals, and weakly bound complexes, where semilocal density functional results exhibit strong functional dependence.

1. INTRODUCTION

Density functional theory (DFT) using semilocal and hybrid functionals is the electronic structure method of choice in most areas of chemistry, solid-state physics, and materials science (1). Despite its popularity, semilocal DFT is increasingly facing a crisis of functional inflation: For example, the latest release of the LIBXC functional library (2) contains well over 300 semilocal density functionals. Functional inflation is, to a large extent, caused by the high sensitivity of semilocal DFT results to the parameterization of the underlying approximate functional, confounding the user and severely limiting predictive power. Parameterized functionals can be surprisingly accurate for certain types of compounds and properties, but fail for others, including a property as basic as the electron density itself (3). Despite recent efforts to consolidate the number of empirical parameters (4), functional inflation remains a vexing problem for many important applications to small-gap compounds such as open-shell d- and f-element complexes (5) or to charge-transfer excitation energies in larger systems (6), where experimental data are scarce and few or no alternatives to semilocal DFT exist.

In the past decade, electronic structure methods based on the random-phase approximation (RPA; see the sidebar titled One Name, Many Methods) have emerged as a possible solution to the functional inflation crisis. RPA methods include part of the electron correlation energy explicitly to capture important physical effects without excessively increasing the computational cost. For example, RPA is the lowest level of theory that correctly describes screening as well as mid- and long-range dispersion interactions without empirical corrections. Unlike single-reference methods based on Hartree–Fock (HF) theory such as second-order Møller–Plesset (MP2) perturbation theory, RPA is insensitive to the size of the noninteracting gap and can even be applied to metallic systems (13). In the context of DFT, RPA may be viewed as the fifth rung on Jacob's ladder of density functional approximations (14), but it is also closely related to coupled-cluster (CC) theory (15), many-body Green's function or propagator methods (16, 17), and time-dependent DFT (TDDFT) (18).

The aim of this review is to introduce RPA methods to newcomers following an intuitive approach. We emphasize physical principles and visualization over formal derivations. Readers interested in the latter are referred to more specialized reviews (19–22). Section 2 outlines the adiabatic-connection fluctuation–dissipation-theorem approach to correlation energy. We then

ONE NAME, MANY METHODS

The term random-phase approximation was first introduced by Bohm & Pines (7) in the context of plasma theory. This approximation was a key step in the transformation from the many-electron Hamiltonian of a uniform electron gas to a simpler Hamiltonian of quasi-electrons with a short-range interaction plus a coupled harmonic oscillator Hamiltonian describing plasma oscillations. Gell-Mann & Brueckner (8) showed in 1957 that in the limit of high electron density, the Bohm–Pines ground-state energy is equivalent to the sum of all ring diagrams in many-body perturbation theory; hence the name ring approximation, which is synonymous with random-phase approximation (RPA). Unlike the Bohm–Pines approach, Gell-Mann & Brueckner's definition of RPA is easily extended to nonuniform systems. In the early 1960s, chemists started to use the term RPA synonymously with time-dependent Hartree–Fock (TDHF) theory, which includes additional ladder diagrams (9, 10). However, unlike the original RPA, the resulting RPA with exchange (RPAX) suffers from instabilities of the HF reference and never thrived as a method for computing ground-state correlation energies (11). To distinguish it from RPAX, RPA is still sometimes called direct or bare RPA. In 1975, Langreth & Perdew (12) introduced RPA in the context of adiabatic connection density functional theory, which remains the most concise and widely accepted definition to date.

introduce RPA from three different perspectives in Section 3. We review recent developments in beyond-RPA corrections, RPA correlation potentials, and efficient RPA energy and analytic gradient implementations in Sections 4 and 5. Section 6 provides examples of possible areas where RPA methods could be applied.

This review is not intended to be exhaustive. Many other advances in electronic structure theory inspired by RPA are not covered herein, including particle–particle or ladder RPA (23–26), range-separation methods (27, 28) and RPA hybrids (29, 30), distinguishable cluster methods (31, 32), many-body dispersion methods (33), and quantum Drude models (34).

2. THEORY

2.1. Adiabatic Connection

The adiabatic connection (AC) uses a single coupling strength parameter α to switch continuously from the noninteracting Kohn–Sham (KS) system (35) ($\alpha = 0$) to the physical many-electron system of interest ($\alpha = 1$). A key aspect of the AC that distinguishes it from other deformations of the physical system is the constraint that the ground-state density be equal to the physical ground-state density ρ for all α. The AC Hamiltonian is thus (12, 36)

$$\hat{H}_\alpha[\rho] = \hat{T}_\mathrm{e} + \hat{V}_\mathrm{ne} + \hat{V}_\alpha[\rho] + \alpha\hat{V}_\mathrm{ee}, \qquad 1.$$

where $\hat{T}_\mathrm{e}$ is the kinetic energy operator, $\hat{V}_\mathrm{ne}$ is the nucleus–electron attraction operator, $\hat{V}_\alpha[\rho]$ is a one-electron local potential operator uniquely determined (up to a constant) by the density constraint (37), and $\hat{V}_\mathrm{ee}$ is the operator of the electron–electron Coulomb interaction; atomic (hartree) units are used throughout this review, i.e., the electron mass, elementary charge, and reduced Planck's constant are set to unity. By construction, $\hat{V}_\alpha[\rho]$ turns into the Hartree, exchange, and correlation (HXC) potential for $\alpha = 0$, and the ground-state wavefunction Ψ_α becomes the KS determinant Φ.

The energy of the physical ground state E is the sum of the energy expectation value of the KS determinant and the correlation energy,

$$E = \langle\Phi|\hat{H}|\Phi\rangle + E^\mathrm{C}. \qquad 2.$$

This definition of the correlation energy is appropriate in a density functional context, whereas the traditional definition in wavefunction theory uses the HF determinant (38).

Using the density constraint, the AC correlation energy may be recast as a coupling strength integral (12, 36):

$$E^\mathrm{C}[\rho] = \int_0^1 \mathrm{d}\alpha \Big(\langle\Psi_\alpha[\rho]\,|\,\hat{V}_\mathrm{ee}\,|\,\Psi_\alpha[\rho]\rangle - \langle\Phi[\rho]\,|\,\hat{V}_\mathrm{ee}\,|\,\Phi[\rho]\rangle \Big). \qquad 3.$$

Equation 3 expresses the correlation energy entirely as an expectation value of the electron–electron Coulomb repulsion $\hat{V}_\mathrm{ee}$; the coupling strength integration automatically takes care of the kinetic correlation energy.

2.2. Fluctuation–Dissipation Theorem

The zero-temperature fluctuation–dissipation theorem (FDT) relates ground-state fluctuations to dissipation in the linear response regime (39). Because electron correlation is related to ground-state density fluctuations (20), the FDT may be used to express the correlation energy as

(12, 40)

$$E^{\mathrm{C}}[\rho] = -\frac{1}{2\pi}\int_0^1 \mathrm{d}\alpha\, \mathrm{Im}\int_0^\infty \mathrm{d}\omega \int \mathrm{d}x\, \mathrm{d}x'\, \frac{\chi_\alpha(x,x',\omega) - \chi_0(x,x',\omega)}{|\mathbf{r}-\mathbf{r}'|}. \quad 4.$$

Here, the frequency-dependent linear density–density response function

$$\chi_\alpha(\omega, x, x') = \left.\frac{\delta\rho(\omega,x)}{\delta v_\alpha(\omega,x')}\right|_{v_\alpha=0} \quad 5.$$

has been introduced, where ω denotes frequency and $x = (\mathbf{r}, \sigma)$ denotes space–spin coordinates. The frequency dependence may be imagined to arise from a frequency-dependent external potential $v^{\mathrm{ext}}(\omega, x')$ perturbing the ground state of $\hat{H}_\alpha$; $v_\alpha(\omega, x')$ is the sum of $v^{\mathrm{ext}}(\omega, x')$ and a time-dependent local potential that arises from the constraint of the time-dependent density to its value at $\alpha = 1$ (41).

A striking feature of Equation 4 is that the correlation energy is expressed in terms of one-electron linear response properties, which are accessible from time-dependent perturbation theory and have been well studied because of their importance, e.g., for spectroscopy.

2.3. Time-Dependent Density Functional Theory

Computing the ground-state correlation energy from the FDT still requires knowledge of the density–density response function at each coupling strength $0 \leqslant \alpha \leqslant 1$. TDDFT (41, 42) provides a conceptually and computationally simple avenue: χ_α may be obtained from the time-dependent KS (TDKS) system instead of the interacting system because their time-dependent densities are the same by construction. Thus, $\chi_\alpha(\omega, x_1, x_2)$ is the diagonal of the TDKS density-matrix–density-matrix response function $\Pi^{\mathrm{s}}_\alpha(\omega, x_1, x_1', x_2, x_2')$ in real space,

$$\chi_\alpha(\omega, x_1, x_2) = \Pi^{\mathrm{s}}_\alpha(\omega, x_1, x_1, x_2, x_2), \quad 6.$$

just as the interacting time-dependent density is the diagonal of the TDKS (one-electron) density matrix.

The TDKS density-matrix–density-matrix response function, or retarded polarization propagator, may be represented by a supermatrix (i.e., a matrix of matrices) (43) of dimension $2N_{\mathrm{ph}} \times 2N_{\mathrm{ph}}$, where N_{ph} is the dimension of the particle–hole (ph) space. A weak external perturbation may excite an electron from some KS occupied orbital ϕ_i to some virtual orbital ϕ_a. In the particle–hole picture, the electron is excited from the KS reference state, or Fermi vacuum, leaving behind a positively charged hole below the Fermi level and creating a negatively charged electron or particle above the Fermi level. The resulting KS particle–hole pair is described by the orbital product $\phi_i(x)\phi_a(x')$, whose diagonal integrates to zero because the excitation conserves the total electron number. Throughout this review, indices $i, j, \ldots$ denote occupied (hole), $a, b, \ldots$ virtual (particle), and $p, q, \ldots$ general KS molecular orbitals. All orbitals are assumed to be real.

Density-matrix response theory yields an expression for the TDKS polarization propagator familiar from TDHF theory (44–46):

$$\boldsymbol{\Pi}^{\mathrm{s}}_\alpha(\omega) = -\left[\begin{pmatrix} \mathbf{A}_\alpha(\omega) & \mathbf{B}_\alpha(\omega) \\ \mathbf{B}_\alpha(\omega) & \mathbf{A}_\alpha(\omega) \end{pmatrix} - (\omega + i\eta)\begin{pmatrix} \mathbf{1} & \mathbf{0} \\ \mathbf{0} & -\mathbf{1} \end{pmatrix}\right]^{-1}. \quad 7.$$

The $i\eta$ contour distortion makes $\boldsymbol{\Pi}^{\mathrm{s}}_\alpha$ analytic in the upper half of the complex frequency plane and thus guarantees causality (47); the limit $\eta \to 0^+$ is taken after a possible frequency integration. $\mathbf{A}_\alpha$ and $\mathbf{B}_\alpha$ are the TDKS orbital rotation Hessians,

$$(A_\alpha + B_\alpha)_{iajb}(\omega) = (\epsilon_a - \epsilon_i)\delta_{ij}\delta_{ab} + 2\alpha B^{\mathrm{H}}_{iajb} + 2(B^{\mathrm{XC}}_\alpha)_{iajb}(\omega), \quad 8.$$

$$(A_\alpha - B_\alpha)_{iajb}(\omega) = (\epsilon_a - \epsilon_i)\delta_{ij}\delta_{ab}, \tag{9.}$$

where ϵ_i and ϵ_a are KS orbital energies,

$$B^{\mathrm{H}}_{iajb} = (ij|ab) = \int \mathrm{d}x_1\, \mathrm{d}x_2\, \phi_i(x_1)\phi_a(x_1)\frac{1}{|\mathbf{r}_1 - \mathbf{r}_2|}\phi_j(x_2)\phi_b(x_2) \tag{10.}$$

is a four-center electron repulsion integral in Mulliken notation, and

$$(B^{\mathrm{XC}}_\alpha)_{iajb}(\omega) = \int \mathrm{d}x_1\, \mathrm{d}x_2\, \phi_i(x_1)\phi_a(x_1) f^{\mathrm{XC}}_\alpha(\omega, x_1, x_2)\phi_j(x_2)\phi_b(x_2) \tag{11.}$$

is a frequency-dependent matrix element of the exchange-correlation (XC) kernel at coupling strength α.

Equation 7 may be written in different forms emphasizing different physical aspects. Defining the supermatrices of the bare Coulomb or Hartree interaction and of the XC kernel, respectively, as

$$\mathbf{V} = \begin{pmatrix} \mathbf{B}^{\mathrm{H}} & \mathbf{B}^{\mathrm{H}} \\ \mathbf{B}^{\mathrm{H}} & \mathbf{B}^{\mathrm{H}} \end{pmatrix}, \qquad \mathbf{F}^{\mathrm{XC}}_\alpha(\omega) = \begin{pmatrix} \mathbf{B}^{\mathrm{XC}}_\alpha(\omega) & \mathbf{B}^{\mathrm{XC}}_\alpha(\omega) \\ \mathbf{B}^{\mathrm{XC}}_\alpha(\omega) & \mathbf{B}^{\mathrm{XC}}_\alpha(\omega) \end{pmatrix}, \tag{12.}$$

we arrive at the Bethe–Salpeter equation (BSE) for $\mathbf{\Pi}^{\mathrm{s}}_\alpha$ (17, 48):

$$\mathbf{\Pi}^{\mathrm{s}}_\alpha(\omega) = \mathbf{\Pi}_0(\omega) + \mathbf{\Pi}_0(\omega)\Big(\alpha\mathbf{V} + \mathbf{F}^{\mathrm{XC}}_\alpha(\omega)\Big)\mathbf{\Pi}^{\mathrm{s}}_\alpha(\omega), \tag{13.}$$

where the bare KS polarization propagator $\mathbf{\Pi}_0$ equals $\mathbf{\Pi}^{\mathrm{s}}_\alpha$ at zero coupling strength. This form emphasizes the screening of $\mathbf{\Pi}_0$ resulting from Hartree and XC interactions. Alternatively, one may focus on the poles of $\mathbf{\Pi}^{\mathrm{s}}_\alpha$, which occur at excitation energies of the α-coupled interacting system. At these excitation energies, the inverse of $\mathbf{\Pi}^{\mathrm{s}}_\alpha$ becomes singular, leading to the TDKS eigenvalue problem:

$$\left[\begin{pmatrix} \mathbf{A}_\alpha(\Omega_{\alpha n}) & \mathbf{B}_\alpha(\Omega_{\alpha n}) \\ \mathbf{B}_\alpha(\Omega_{\alpha n}) & \mathbf{A}_\alpha(\Omega_{\alpha n}) \end{pmatrix} - \Omega_{\alpha n}\begin{pmatrix} \mathbf{1} & \mathbf{0} \\ \mathbf{0} & -\mathbf{1} \end{pmatrix}\right]\begin{pmatrix} \mathbf{X}_{\alpha n} \\ \mathbf{Y}_{\alpha n} \end{pmatrix} = \mathbf{0}, \quad \mathbf{X}^{\mathrm{T}}_{\alpha n}\mathbf{X}_{\alpha n} - \mathbf{Y}^{\mathrm{T}}_{\alpha n}\mathbf{Y}_{\alpha n} = \mathbf{1}. \tag{14.}$$

For $\alpha = 1$, the eigenvalues equal electronic excitation energies of the physical system, and the eigenvectors yield the corresponding transition densities, which is key for TDDFT applications to electronic spectroscopy (42).

Finally, the correlation energy may be expressed in terms of $\mathbf{\Pi}^{\mathrm{s}}_\alpha$,

$$E^{\mathrm{C}} = -\frac{1}{2\pi}\int_0^1 \mathrm{d}\alpha\, \mathrm{Im}\int_0^\infty \mathrm{d}\omega \Big\langle \mathbf{V}\Big(\mathbf{\Pi}^{\mathrm{s}}_\alpha(\omega) - \mathbf{\Pi}_0(\omega)\Big)\Big\rangle, \tag{15.}$$

where angle brackets denote the trace operation. However, computation of $\mathbf{\Pi}^{\mathrm{s}}_\alpha$ requires knowledge of the XC kernel. As explained below, Equation 15 is more than a complicated reformulation of the problem that shifts the difficulty from the XC energy to the kernel.

3. RANDOM-PHASE APPROXIMATION

3.1. Time-Dependent Density Functional Theory Perspective

Within RPA, the XC kernel in Equation 13 is entirely neglected; this is equivalent to the time-dependent Hartree approximation. Thus, $\mathbf{\Pi}^{\mathrm{s}}_\alpha$ is approximated by

$$\mathbf{\Pi}^{\mathrm{RPA}}_\alpha(\omega) = \mathbf{\Pi}_0(\omega) + \alpha\mathbf{\Pi}_0(\omega)\mathbf{V}\mathbf{\Pi}^{\mathrm{RPA}}_\alpha(\omega). \tag{16.}$$

Defining the dimensionless generalized dielectric function (47) within RPA as $\boldsymbol{\kappa}_\alpha^{\mathrm{RPA}}(\omega) = 1 - \alpha\boldsymbol{\Pi}_0(\omega)\mathbf{V}$, the BSE for $\boldsymbol{\Pi}_\alpha^{\mathrm{RPA}}$ (Equation 16) becomes

$$\boldsymbol{\Pi}_\alpha^{\mathrm{RPA}}(\omega) = \left(\boldsymbol{\kappa}_\alpha^{\mathrm{RPA}}(\omega)\right)^{-1}\boldsymbol{\Pi}_0(\omega). \quad 17.$$

This affords an appealing physical interpretation: $\boldsymbol{\kappa}_\alpha^{\mathrm{RPA}}(\omega)$ accounts for screening of bare KS particle–hole pairs resulting from other induced particle–hole pairs, i.e., polarization, through the Hartree interaction. In other words, $\boldsymbol{\Pi}_\alpha^{\mathrm{RPA}}$ is dressed or renormalized by the interaction between particle–hole pairs. Alternatively, the effect of screening may be illustrated by defining the RPA effective interaction

$$\mathbf{V}_\alpha^{\mathrm{RPA}}(\omega) = \mathbf{V} + \alpha\mathbf{V}\boldsymbol{\Pi}_0(\omega)\mathbf{V}_\alpha^{\mathrm{RPA}}(\omega) = \mathbf{V}\left(\boldsymbol{\kappa}_\alpha^{\mathrm{RPA}}(\omega)\right)^{-1}. \quad 18.$$

Without screening, $\boldsymbol{\kappa}_0^{\mathrm{RPA}} = 0$, and $\mathbf{V}_\alpha^{\mathrm{RPA}}(\omega)$ reduces to the Hartree interaction, which is instantaneous. However, for finite α, $\mathbf{V}_\alpha^{\mathrm{RPA}}(\omega)$ acquires frequency dependence because of screening by induced particle–hole pairs.

To avoid singularities of the polarization propagators near the real axis, we may perform the frequency integration in Equation 15 along the imaginary axis using Cauchy's integral theorem (49). Analytically integrating over the coupling strength then yields an expression for the RPA correlation energy solely in terms of the KS polarization propagator and the Hartree interaction (40):

$$E^{\mathrm{C\,RPA}} = \frac{1}{2\pi}\int_0^\infty \mathrm{d}\omega \left\langle \ln\left(\mathbf{1} - \boldsymbol{\Pi}_0(i\omega)\mathbf{V}\right) + \boldsymbol{\Pi}_0(i\omega)\mathbf{V}\right\rangle. \quad 19.$$

For closed-shell systems at large separation, Equation 19 correctly accounts for dispersion interactions at the coupled-monomer level, thereby providing a generalization of dispersion interactions for systems of finite size (see References 22, 50 and the sidebar titled Dispersion Forces).

3.2. Plasmon Perspective

A particularly simple representation of the RPA correlation energy results from performing both the frequency and coupling strength integrations in Equation 15 analytically (54),

$$E^{\mathrm{C\,RPA}} = \frac{1}{2}\sum_n \left(\Omega_n^{\mathrm{RPA}} - \Omega_n^{\mathrm{RPA1}}\right); \quad 20.$$

here Ω_n^{RPA} and Ω_n^{RPA1} are the RPA electronic excitation energies and those to first order in α, respectively, and the summation includes all excitations. In the spirit of Bohm & Pines's work, the plasmon formula (Equation 20) states that the RPA correlation energy is the difference between

DISPERSION FORCES

Dispersion interactions arise from long-range interactions between spontaneous dipole moment fluctuations of monomers. RPA provides a seamless generalization of this physical picture to electron interactions at finite range (22, 50) because it is based on correlated fluctuations of the entire electron density (Equation 19) rather than monomer multipoles. Thus, RPA may be applied to systems with strong intramolecular dispersion interactions, such as sterically crowded compounds, transition states, and molecular crystals. By contrast, dispersion methods based on intermolecular perturbation theory, such as corrections using uncoupled dispersion coefficients or symmetry adapted perturbation theory (51–53), may diverge for these systems.

the zero-point oscillation energies of electronic excitations at full coupling and those to first order in the electron interaction. In this picture, each excitation represents one harmonic degree of freedom. The sum in Equation 20 is dominated by excitations whose energies change most as the interaction is turned on; this is a key characteristic of plasmons (55). Plasmons are long-wavelength oscillations of an electron gas and are highly collective, i.e., they involve oscillations of the entire electron gas and cannot be described by single KS particle–hole pairs or single-electron excitations.

The connection between the RPA correlation energy and collective excitations becomes especially clear by further rewriting Equation 20 as

$$E^{\mathrm{C\,RPA}} = -\frac{1}{2}\sum_n \Omega_n^{\mathrm{p}}, \qquad 21.$$

where Ω_n^{p} are the eigenvalues of $\mathbf{W}^{\mathrm{p}}$, the sum of the second- and higher-order terms of $-(\mathbf{M}_\alpha^{\mathrm{RPA}})^{1/2}$ with respect to α, and $\mathbf{M}_\alpha^{\mathrm{RPA}}$ is the reduced RPA orbital rotation Hessian (56),

$$\mathbf{M}_\alpha^{\mathrm{RPA}} = \left(\mathbf{A}_\alpha^{\mathrm{RPA}} - \mathbf{B}_\alpha^{\mathrm{RPA}}\right)^{1/2}\left(\mathbf{A}_\alpha^{\mathrm{RPA}} + \mathbf{B}_\alpha^{\mathrm{RPA}}\right)\left(\mathbf{A}_\alpha^{\mathrm{RPA}} - \mathbf{B}_\alpha^{\mathrm{RPA}}\right)^{1/2}. \qquad 22.$$

$\mathbf{W}^{\mathrm{p}}$ can be shown to be positive definite. Typically, a few large eigenvalues of $\mathbf{W}^{\mathrm{p}}$ dominate the RPA correlation energy, and the corresponding eigenvectors may be interpreted as plasmonic modes describing collective excitations of the electrons that give rise to large zero-point energies.

We illustrate the plasmonic mode analysis of the RPA correlation energy for the tetrahedral Ag_{20} cluster (57) in **Table 1** and **Figure 1**. The modes with the largest 10 eigenvalues make up over 90% of the total RPA correlation energy in a split valence plus polarization (SVP) atomic orbital (AO) basis (see **Table 1**). Visualization of the modes (see **Figure 1**) shows that those with the largest contributions to the correlation energy are highly collective, i.e., they involve oscillations of the entire electron cloud of the cluster. These collective modes have few nodes, in accord with the notion that plasmons are low-wavelength excitations. The plasmonic modes are poorly described by either KS single-orbital or RPA excitations, but they provide an efficient representation of the RPA correlation energy.

Table 1 Plasmonic modes of Ag_{20} with the 10 largest eigenvalues and their percentage contribution to $E^{\mathrm{C\,RPA}}$

Mode	Eigenvalue (hartree)	% of $E^{\mathrm{C\,RPA}}$
$1A_1$	0.2070	11.5
$2A_1$	0.1836	10.2
$3A_1$	0.1612	8.9
$4A_1$	0.1118	6.6
$1E$	0.1702	9.4
$1T_1$	0.1658	9.2
$1T_2$	0.1728	9.6
$2T_2$	0.1666	9.2
$3T_2$	0.1338	9.1
$4T_2$	0.1467	8.1

Here, the def2-SVP basis set (58) and scalar relativistic small-core pseudopotentials (59) were used; orbitals were generated using the TPSS functional (60) and quadrature grids of size m5 (61). Abbreviations: TPSS, Tao–Perdew–Staroverov–Scuseria; $E^{\mathrm{C\,RPA}}$, random-phase approximation correlation energy.

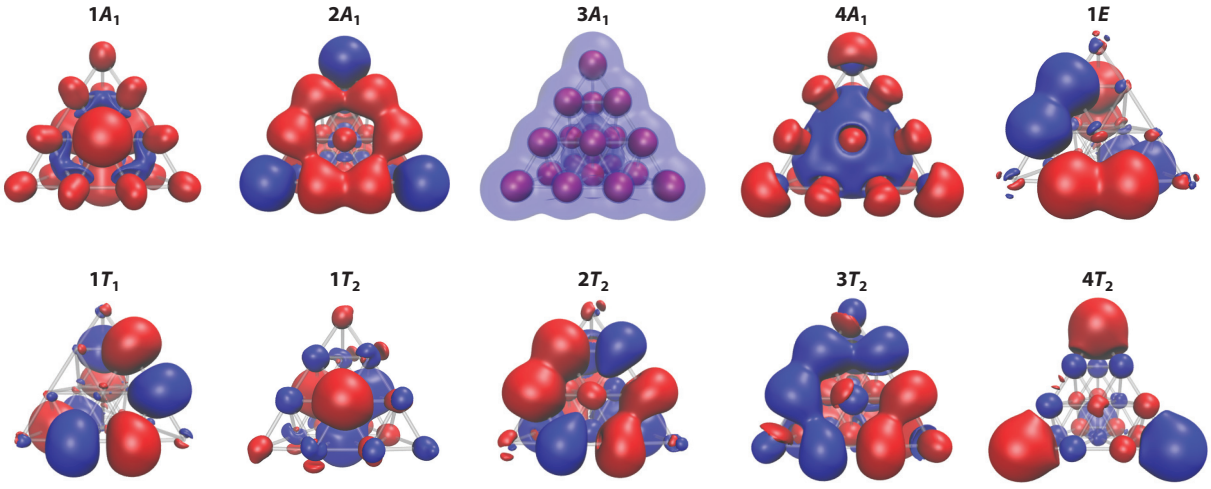

Figure 1

Contour plots of the 10 dominant plasmonic modes of Ag_{20}. Contour values of 0.001 (*red*) and −0.001 (*blue*) were used; only one column is shown for degenerate modes. For further details, see **Table 1**.

3.3. Diagrammatic Perspective

An alternative approach to the density–density response function χ_α uses the interacting polarization propagator $\mathbf{\Pi}_\alpha$ (43). Although both $\mathbf{\Pi}_\alpha$ and the TDKS polarization propagator $\mathbf{\Pi}^s_\alpha$ yield the same density–density response function and thus the same correlation energy through the FDT, the two are not equal (62). $\mathbf{\Pi}_\alpha$ satisfies its own BSE (63),

$$\mathbf{\Pi}_\alpha(\omega) = \mathbf{\Pi}_0(\omega) + \mathbf{\Pi}_0(\omega)\Big(\alpha\mathbf{V} + \mathbf{K}_\alpha(\omega)\Big)\mathbf{\Pi}_\alpha(\omega), \qquad 23.$$

where $\mathbf{K}_\alpha$ is a frequency-dependent kernel accessible, e.g., through many-body perturbation theory and Green's function methods (17, 47). In this many-body theory approach, RPA amounts to neglecting $\mathbf{K}_\alpha$.

In keeping with the Goldstone approach to diagrammatic perturbation theory (64–66), polarization propagators and the Hartree interaction are represented by pairs of arrowed lines and by wiggly lines, respectively (see **Figure 2*a***), and the BSE within the RPA takes the form shown in **Figure 2*b***. The RPA correlation energy can be represented by the bubble diagrams in **Figure 2*c***, again suggesting a physical picture of vacuum fluctuations giving rise to correlation. Substituting **Figure 2*b*** into **Figure 2*c***, integrating over coupling strength, and collecting equivalent diagrams produces the series of ring diagrams first identified by Gell-Mann & Brueckner (8) (see **Figure 2*d***).

4. IMPROVEMENTS AND EXTENSIONS

4.1. Kernel Corrections

The RPA is equivalent to the Hartree approximation for the TDDFT and BSE kernels, and thus lacks any second- or higher-order exchange. As a result, same-spin particle–hole pairs do not experience Pauli repulsion and are screened as much as opposite-spin particle–hole pairs. This makes the RPA on-top correlation hole too negative and leads to overcorrelation of electrons at short interelectron distances (67). In other words, RPA contains spurious self-correlation error,

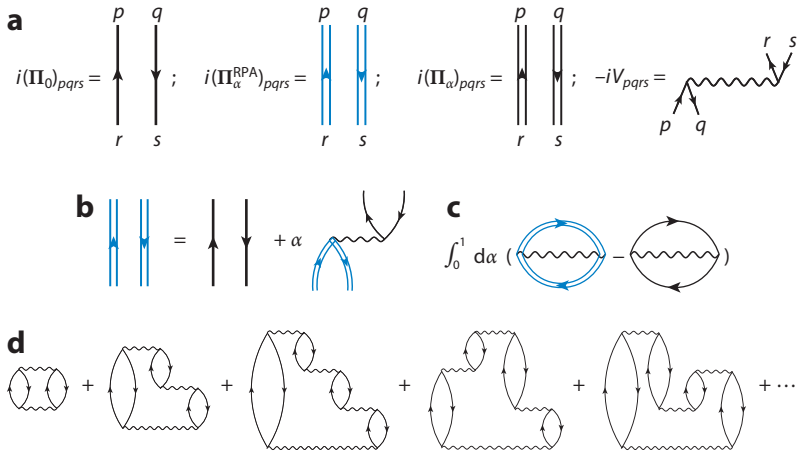

Figure 2

Goldstone diagrams for (*a*) noninteracting and interacting polarization propagators and the bare Coulomb interaction, (*b*) the BSE for $\mathbf{\Pi}_\alpha^{\mathrm{RPA}}$, and (*c*,*d*) the RPA correlation energy (*c*) before and (*d*) after coupling strength integration. For illustrative purposes, we use blue and black double lines to indicate RPA and exact renormalization, respectively; a pair of disconnected double lines should not be understood as a product of single-particle quantities. Abbreviations: BSE, Bethe–Salpeter equation; RPA, random-phase approximation.

which underlies, e.g., its failure to correctly dissociate odd-electron systems such as H_2^+ (25, 68). The unphysical short-range behavior of RPA also explains its relatively poor accuracy for nonisogyric processes, such as atomization, ionization, and spin-flip processes, which break up electron pairs and lead to large changes in the short-range correlation energy (20).

The second-order screened exchange (SOSEX) method by Freeman & Kresse (69, 70) completely eliminates self-correlation error for one-electron systems. The AC-SOSEX beyond-RPA correlation energy (71) is

$$\Delta E^{\mathrm{C\,AC\text{-}SOSEX}} = -\frac{1}{2\pi}\int_0^1 \mathrm{d}\alpha \cdot \alpha\, \mathrm{Im}\int_0^\infty \mathrm{d}\omega \left\langle \mathbf{V}\mathbf{\Pi}_\alpha^{\mathrm{RPA}}(\omega)\mathbf{K}\mathbf{\Pi}_0(\omega)\right\rangle, \qquad 24.$$

where

$$\mathbf{K} = \begin{pmatrix} \mathbf{B}^{\mathrm{X}} & \mathbf{B}^{\mathrm{X}} \\ \mathbf{B}^{\mathrm{X}} & \mathbf{B}^{\mathrm{X}} \end{pmatrix} \qquad 25.$$

is an approximation to the first-order exchange kernel and $B^{\mathrm{X}}_{iajb} = -(ib|ja)$ is the corresponding particle–hole exchange integral. SOSEX partially screens the second-order exchange (see **Figure 3*b***), and is thus useful for small-gap systems and even metals, as opposed to unscreened perturbation theory (69, 72). However, SOSEX does not consistently improve RPA atomization energies, and it worsens the description of reaction barriers and systems with strong static correlation compared to RPA (68).

Systematic improvement is possible by RPA-renormalized many-body perturbation theory (68). The key idea is to expand the exact polarization propagator in terms of the RPA polarization propagator

$$\mathbf{\Pi}_\alpha(\omega) = \mathbf{\Pi}_\alpha^{\mathrm{RPA}}(\omega) + \mathbf{\Pi}_\alpha^{\mathrm{RPA}}(\omega)\mathbf{K}_\alpha(\omega)\mathbf{\Pi}_\alpha(\omega), \qquad 26.$$

diagrammatically represented in **Figure 3*d***. Because RPA is well-behaved for small-gap systems, this expansion avoids the instabilities of conventional many-body perturbation theory by

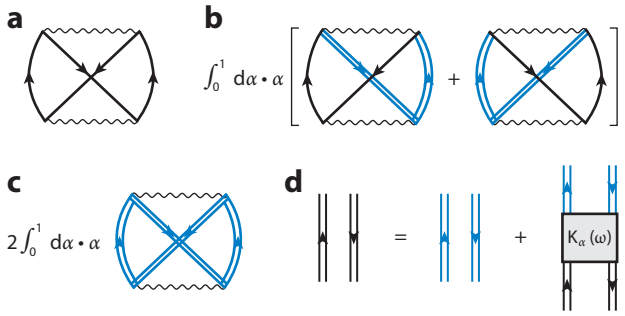

Figure 3

Goldstone diagrams for (*a*) bare second-order exchange energy, (*b*) AC-SOSEX beyond-RPA correlation energy, (*c*) AXK beyond-RPA correlation energy, and (*d*) RPA-renormalized BSE. Abbreviations: AC, adiabatic connection; AXK, approximate exchange kernel; BSE, Bethe–Salpeter equation; RPA, random-phase approximation; SOSEX, second-order screened exchange.

RPA-renormalizing all particle–hole pairs. Using a frequency-independent approximate exchange kernel (AXK), $\mathbf{K}_\alpha^{\mathrm{AXK}} = \alpha\mathbf{K}$, we obtain the AXK second-order beyond-RPA correlation energy (see **Figure 3*c***):

$$\Delta E^{\mathrm{C\,AXK}} = -\frac{1}{2\pi}\int_0^1 \mathrm{d}\alpha \cdot \alpha\,\mathrm{Im}\int_0^\infty \mathrm{d}\omega \left\langle \mathbf{V}\boldsymbol{\Pi}_\alpha^{\mathrm{RPA}}(\omega)\mathbf{K}\boldsymbol{\Pi}_\alpha^{\mathrm{RPA}}(\omega)\right\rangle. \quad 27.$$

Although AXK still contains some self-correlation error, it dissociates covalent bonds correctly and consistently improves upon RPA (68).

4.2. Exchange-Correlation Potentials from the Random-Phase Approximation

The RPA correlation energy (Equation 19) is a functional of the noninteracting KS orbitals and orbital energies. For wavefunction methods, such reference-state dependence is undesirable, as the exact ground-state energy is invariant under any orbital rotations (73). In DFT, by contrast, the KS determinant is unique in the sense that it yields the correct density (given that the density is pure-state noninteracting v-representable). Thus, the problem shifts from achieving reference-state independence to approximating the exact KS potential as accurately as possible.

In the optimized effective potential (OEP) approach (74), a functional of the KS orbitals is minimized under the constraint that the orbitals solve KS equations with a local one-electron potential; this is equivalent to minimization with respect to a one-electron density. Applying the functional derivative chain rule, the local RPA correlation potential is obtained by differentiating the RPA energy functional with respect to the density (75).

RPA correlation potentials of noble gas atoms are more accurate than second-order Görling–Levy (76), local density approximation, or generalized gradient approximation (77) potentials. RPA-OEP misses the derivative discontinuity at odd-integer particle numbers but cancels the fractional spin error in the exchange-only functional (78). In addition, the highest occupied molecular orbital (HOMO) energies, obtained using RPA-OEP, agree well with the exact ionization potentials (79). The OEP methodology has been extended to nonzero kernel corrections beyond RPA (80). However, OEP can be considered an inverse problem and, in conjunction with finite basis sets, has been hampered by numerical instability (81–83). Despite recent attempts to address this issue (84, 85), applications of the RPA-OEP method to large molecular systems remain challenging.

5. IMPLEMENTATIONS

5.1. Random-Phase Approximation Energy Computations

Brute-force computation of the RPA correlation energy using the plasmon formula (Equation 20) requires diagonalization of the $N_{\mathrm{ph}} \times N_{\mathrm{ph}}$ matrix $\mathbf{M}^{\mathrm{RPA}}$ (56). Because both the number of particle (unoccupied) orbitals and the number of hole (occupied) orbitals increase linearly with the system size N in a finite basis set, the operation count of this approach scales as $\mathcal{O}(N^6)$ and quickly becomes prohibitive. Alternatively, the RPA correlation energy may be obtained by retaining only ring contractions in a coupled-cluster doubles (CCD) implementation (15), which scales as $\mathcal{O}(N^6)$ in each CCD iteration.

Low-scaling algorithms are achievable by use of the resolution-of-the-identity (RI) approximation (86) to factorize the electron repulsion integrals (ERIs) according to

$$B^{\mathrm{H}}_{iajb} = (ia \mid jb) = \sum_{PQ} (ia \mid P)(\mathbf{U}^{-1})_{PQ}(Q \mid jb), \qquad 28.$$

where $U_{PQ} = (P|Q)$ is a two-center ERI. This factorization states that the KS particle–hole transition densities may be represented by (nonorthonormal) auxiliary basis functions $P, Q, \ldots$ using the inner product defined by ERIs. With finite auxiliary basis, Equation 28 is equivalent to the so-called density fitting in the Coulomb metric or the least-squares fitting of electrostatic fields generated by particle–hole pairs (87). The RI approximation can be highly accurate with atom-centered auxiliary basis sets ~3–5 times the size of the corresponding AO basis sets. Auxiliary basis sets optimized for RI-MP2 energies (88) lead to errors on the order of 10 μHa per atom in RPA calculations, which is below the inherent method error in typical applications (89).

With the RI approximation, the scaling of ring-CCD calculations may be reduced to $\mathcal{O}(N^4)$ (90), but the solution is obtained using iterative methods and requires storage of large cubic-scaling arrays. Alternatively, the RI approximation may be applied to the RPA correlation energy (Equation 19 or 20) along with numerical frequency integration (89):

$$E^{\mathrm{C\ RI\text{-}RPA}} = \frac{1}{2\pi} \int_0^\infty \mathrm{d}\omega \langle \ln(\mathbf{1} + \mathbf{Q}(\omega)) - \mathbf{Q}(\omega) \rangle, \qquad 29.$$

where $\mathbf{Q}$ is represented in an auxiliary basis and corresponds to the bare KS polarization propagator dressed by the Hartree interaction. Using a Clenshaw–Curtis quadrature for the numerical integration (91), the evaluation of the RI-RPA correlation energy scales as $\mathcal{O}(N^4)$. If a system-independent energy error is desired, e.g., for reaction energy calculations, finer quadratures are required for larger systems, introducing an extra $\mathcal{O}(\ln N)$ scaling factor. In practice, however, a quadrature of ≤100 points is adequate for most small and medium-sized molecules.

Further lowering of the computational complexity has been achieved by factorization of $\mathbf{\Pi}_0$ using Laplace transform (92, 93) and frequency-domain (94) techniques with density fitting in the least-squares (or overlap) metric (95) or tensor hypercontraction (96), and by local-domain coupled-cluster methods (97). These algorithms scale favorably for very large systems, but come at the cost of larger prefactors compared to higher-scaling approaches and, in some cases, additional parameters. Thus, the quartic scaling algorithm may be more efficient than lower-scaling alternatives up to well above 100 atoms in typical applications. **Figure 4** displays timings for large organic molecules from the S12L test set (98) using the RI-RPA implementation available in Turbomole V7.0; the effective scaling is subquartic.

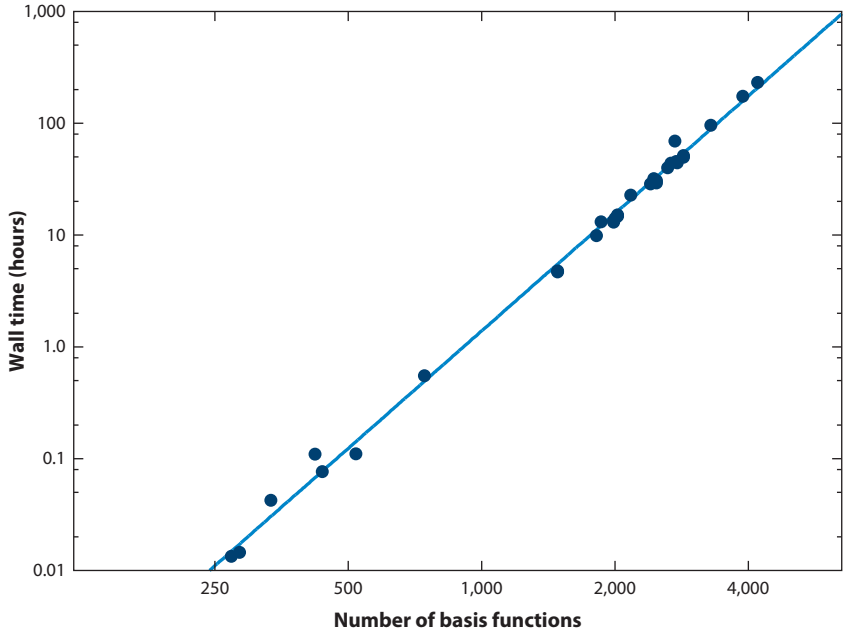

Figure 4

Wall times in hours for single-point RI-RPA energy calculations on S12L test set (98) plotted versus system size. The PBE functional (99, 100) and the def2-TZVP basis set (58) were used to generate the KS reference; 100 quadrature points were used for numerical frequency integration. All RI-RPA calculations were performed with 5,000 MiB reserved memory on one core of a Xeon E5-2680 v2 2.8-GHz processor. The largest system contains 158 atoms. Timings include the cost of calculating the exact exchange energy. The slope of the regression line is 3.49. Abbreviations: KS, Kohn–Sham; PBE, Perdew–Burke–Ernzerhof; TZVP, triple-zeta valence plus polarization; RI-RPA, resolution-of-the-identity random-phase approximation.

5.2. Analytic Gradients Within the Random-Phase Approximation

Analytic energy gradients are a prerequisite for molecular structure optimization and property calculations (101). For energies that are variationally determined, their gradients can be efficiently evaluated by virtue of the Hellmann–Feynman theorem. Although the RPA energy functional E^{RPA} is not variational, a Lagrangian can be constructed for computing energy gradients without solving for perturbed KS orbitals (102, 103):

$$L^{\mathrm{RPA}}(\mathbf{C}, \boldsymbol{\epsilon}, \mathbf{D}^{\Delta}, \mathbf{W} \,|\, \mathbf{h}, \mathbf{v}, \mathbf{V}^{\mathrm{XC}}, \mathbf{S}) = E^{\mathrm{RPA}}(\mathbf{C}, \boldsymbol{\epsilon} \,|\, \mathbf{h}, \mathbf{v}) + \left\langle \mathbf{D}^{\Delta}(\mathbf{C}^{\mathrm{T}}\mathbf{F}\mathbf{C} - \boldsymbol{\epsilon}) \right\rangle - \left\langle \mathbf{W}(\mathbf{C}^{\mathrm{T}}\mathbf{S}\mathbf{C} - \mathbf{1}) \right\rangle. \quad 30.$$

This RPA Lagrangian depends on orbital coefficients $\mathbf{C}$ and a matrix $\boldsymbol{\epsilon}$ that reduces to the diagonal matrix of orbital energies for the input KS solution, as well as on the Lagrange multipliers $\mathbf{D}^{\Delta}$ and $\mathbf{W}$; additionally, L^{RPA} depends parametrically on the one- and two-electron integrals $\mathbf{h}$ and $\mathbf{v}$, the ground-state XC potential matrix $\mathbf{V}^{\mathrm{XC}}$, and the overlap matrix $\mathbf{S}$, all in an AO basis (104). The Fock matrix $\mathbf{F}$ is the effective one-electron KS Hamiltonian and can be expressed in terms of $\mathbf{h}$, $\mathbf{v}$, and $\mathbf{V}^{\mathrm{XC}}$.

By construction, the correct RPA energy for given KS orbitals and orbital energies is attained by unconstrained optimization of the RPA Lagrangian. The variation with respect to $\mathbf{D}^{\Delta}$ enforces

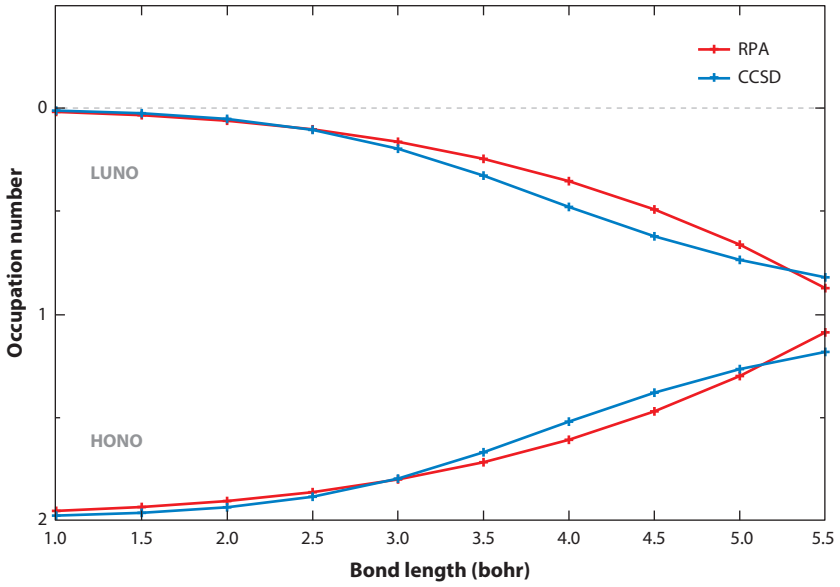

Figure 5

Natural orbital occupation numbers of the HONO and LUNO of ground-state H_2 using spin-restricted RPA with a PBE reference and CCSD as a function of interatomic distance. The aug-cc-pV5Z basis set (108) was used. An orbital is considered occupied if the occupation is >1, and unoccupied if the occupation is <1. Abbreviations: CCSD, coupled-cluster singles and doubles; HONO, highest occupied natural orbital; LUNO, lowest unoccupied natural orbital; PBE, Perdew–Burke–Ernzerhof; RPA, random-phase approximation.

that $\mathbf{C}$ and $\boldsymbol{\epsilon}$ satisfy the KS equations

$$\mathbf{C}^{\mathrm{T}}\mathbf{F}\mathbf{C} = \boldsymbol{\epsilon}, \tag{31.}$$

and the variation with respect to $\mathbf{W}$ recovers the orthonormality constraint

$$\mathbf{C}^{\mathrm{T}}\mathbf{S}\mathbf{C} = \mathbf{1}. \tag{32.}$$

The corresponding constraint terms in L^{RPA} may be viewed as energetic penalties for violating the constraints, and they both vanish at the stationary point. The total differential of L^{RPA} reveals the physical meaning of the Lagrange multipliers (104): $\mathbf{D}^{\Delta}$ corresponds to a correction to the KS density matrix $\mathbf{D}^{\mathrm{KS}}$ due to correlation and orbital relaxation, and $\mathbf{W}$ is the energy weighted density matrix (105). The RPA density matrix

$$\mathbf{D}^{\mathrm{RPA}} = \frac{\mathrm{d}E^{\mathrm{RPA}}}{\mathrm{d}\mathbf{h}} = \mathbf{D}^{\mathrm{KS}} + \mathbf{C}\mathbf{D}^{\Delta}\mathbf{C}^{\mathrm{T}} \tag{33.}$$

facilitates the analysis of RPA calculations in terms of natural orbitals and occupation numbers. Within a spin-restricted formalism, the RPA natural orbitals of stretched H_2 exhibits significant fractional occupation, which resembles the exact solution from coupled-cluster singles and doubles (CCSD) (see **Figure 5**). This result agrees with prior observations that RPA is capable of partially capturing static correlation (56, 106, 107).

The stationarity of the Lagrangian ensures that the orbitals and orbital energies satisfy Wigner's $2n + 1$ rule, and the Lagrange multipliers satisfy a stronger $2n + 2$ rule (103). Thus, it is not necessary to solve coupled perturbed KS (CPKS) equations for each perturbation; instead, the Lagrange multipliers can be determined by solving a single set of CPKS equations. With the

RI approximation, numerical frequency integration, ERI prescreening techniques, and iterative subspace methods (109, 110), the RPA energy gradient implementation in Turbomole has achieved the same $\mathcal{O}(N^4 \ln N)$ scaling as single-point RPA energy calculations. In a typical application, the computational cost for a gradient vector with respect to all nuclear displacements is ~5 times that for the corresponding RPA energy. Routine RPA molecular structure optimizations are feasible for systems with ~100 atoms using triple- or quadruple-zeta basis sets on single workstation computers (104).

Other recent implementations of RPA analytic gradients (111, 112) are based on the ring-CCD formulation with a HF reference and scale as $\mathcal{O}(N^6)$. Analytic energy gradients were also implemented for range-separated hybrid functionals with short-range semilocal approximation and long-range RPA (112).

6. APPLICATIONS

6.1. Gold Clusters

Despite the chemical inertness of bulk gold (113), small gold clusters supported on a metal oxide surface are excellent catalysts (114, 115), and their activity is believed to be related to the dimensionality of their structures, which changes from two-dimensional (2D) to three-dimensional (3D) with increasing cluster size (116). The 2D–3D crossover points of gold cluster cations and anions are well established to occur at cluster sizes of 8 atoms (117) and 12 atoms (118), respectively. For neutral clusters, experimental studies suggest that Au_7 and Au_8 are still planar (118a, 119); theoretical estimates for the 2D–3D crossover point range from 7 to 14 atoms (119a–122).

To obtain an accurate estimate of the 2D–3D crossover point for neutral gold clusters, a genetic algorithm (123) based on TPSS (60) potential energy surfaces was used to identify low-energy isomers (124). Relative energies of these isomers were determined by single-point calculations using revTPSS (125) and RPA; the latter is well suited for gold clusters, where the noninteracting gap is small and dispersion interactions may be important. Thermal, scalar relativistic, and spin-orbit corrections were included. The methodology was validated for the known crossover points of gold cluster anions and cations. Isomers III (2D) and I (3D) of Au_{11} (see **Figure 6**) were found to be almost isoenergetic; clusters with up to 10 atoms are 2D, whereas clusters larger than 11 atoms are manifestly 3D. The unusually large size for 2D–3D crossover in Au clusters compared to Cu and Ag clusters has been attributed to relativistic effects (126).

6.2. Lanthanide and Actinide Complexes

Lanthanides (Ln) form ionic bonds due to the limited radial extension of $4f$ orbitals; thus, the coordination number largely depends on the ionic radius. However, recent experiments on Ln/Ln′ heterobimetallic tuck-over hydride complexes (**Figure 7**) (127) suggested that the smaller metal ion in these complexes is located in the eight-coordinate site rather than the seven-coordinate site. Although semilocal DFT calculations supported this observation for the Y/Lu–Lu/Y mixture, they failed to reproduce the experimental metal ion configurations for the Y/La and Lu/La complexes. Including Grimme's dispersion correction (D3) (128) overcorrected the energy differences between the Ln/Ln′ and Ln′/Ln complexes, whereas RPA correctly reflected the experimental trend (127).

Semilocal and hybrid DFT, RPA, and AXK calculations on the uranium complex $[(C_5H_5)_3U]^-$ suggested a quintet $5f^3 6d^1$ ground-state configuration (**Table 2**), corroborating the semilocal DFT calculations on $[(C_5H_4SiMe_2)_3U]^-$, which is the first isolable U(II) complex (129, 130).

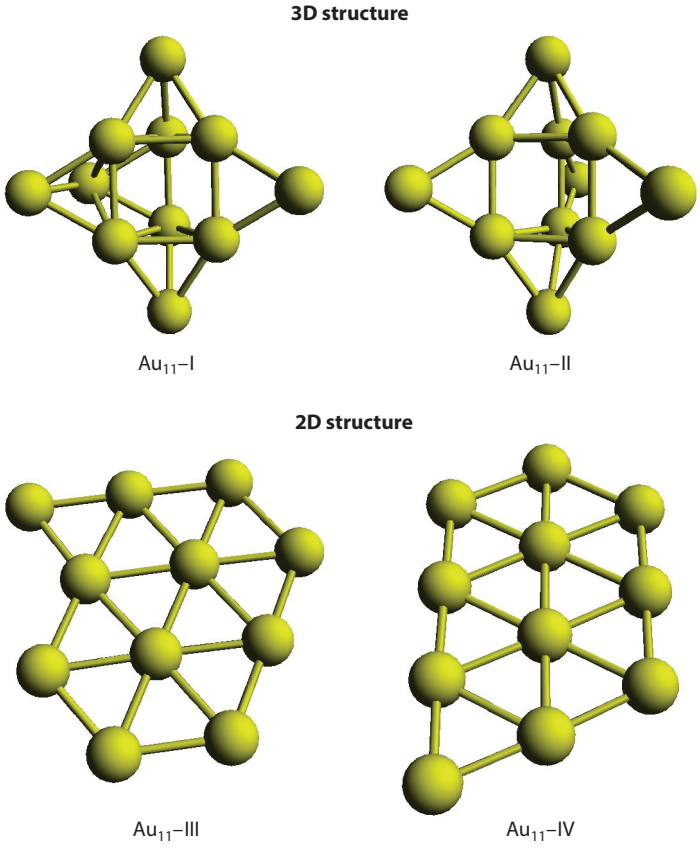

Figure 6

The low-energy two- and three-dimensional (2D and 3D) structures of Au_{11}. Figure adapted from Reference 124 with permission. Copyright 2014 American Chemical Society.

Although both semilocal DFT and RPA methods gave the same trend for the stability of spin states, the semilocal DFT triplet–quintet energy difference varies considerably with the choice of functionals, e.g., 8.5 kcal/mol for TPSS (0% exact exchange) and 12.7 kcal/mol for B3LYP (20% exact exchange) (131, 132). This study illustrates the use of RPA methods for calibrating semilocal DFT results for new compounds for which no precedent or empirical calibration exists.

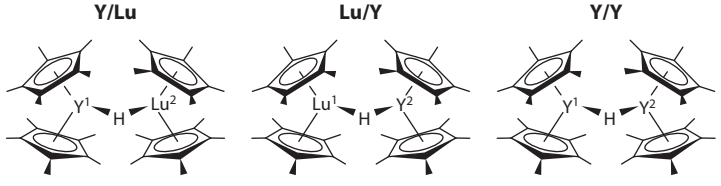

Figure 7

Ln/Ln′ heterobimetallic tuck-over hydride complexes $Cp^*_2Ln(\mu\text{-}H)(\mu\text{-}\eta^1{:}\eta^5\text{-}CH_2C_5Me_4)Ln'Cp^*$, where $Cp^* = C_5Me_5$. Figure adapted from Reference 127 with permission. Copyright 2014 American Chemical Society.

Table 2 Energy difference between triplet and quintet states of $[(C_5H_5)_3U]^-$ using the def2-TZVP basis set

	TPSS	TPSSh	B3LYP	RPA	AXK
ΔE	8.5	10.4	12.7	5.5	5.7

Abbreviations: AXK, approximate exchange kernel; RPA, random-phase approximation; TPSS, Tao–Perdew–Staroverov–Scuseria; TPSSh, Tao–Perdew–Staroverov–Scuseria hybrid; B3LYP, Becke 3-parameter Lee–Yang–Parr.

6.3. Stereoselective Transition States

Diastereoselective reactions are an important class of reactions in the synthesis of natural products that involve multiple stereocenters. In these reactions, one diastereomer is formed selectively over the other because of a difference in the free energy of the transition states. RPA and semilocal DFT were used to study the diastereoselectivity of radical coupling reactions of acetonide radicals and electrophilic alkenes (133) (see **Figure 8**). Similar reactions are encountered in the total synthesis of (−)-chromodorolide B (133a), a rearranged spongian diterpenoid with 10 contiguous stereocenters. Simple rules of steric hindrance fail to predict the relative free energies

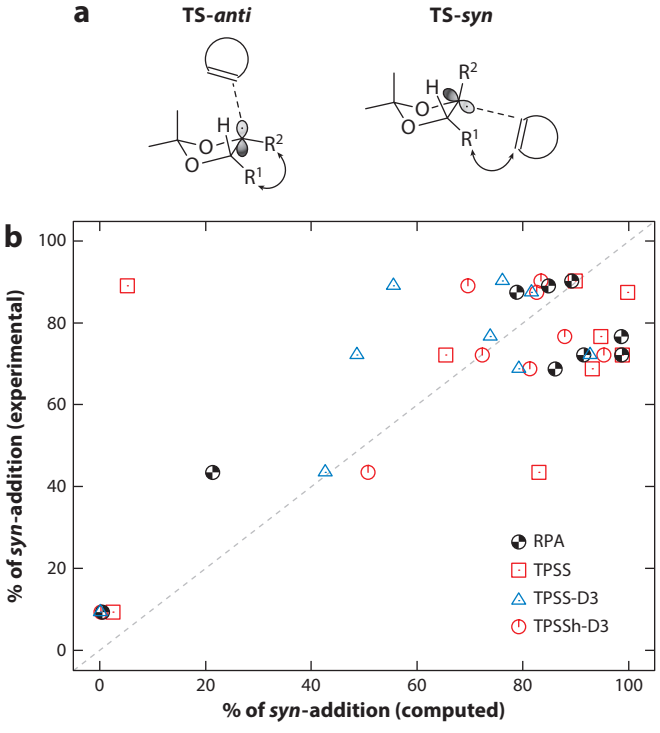

Figure 8

(*a*) TS models for *anti* (TS-*anti*) and *syn* (TS-*syn*) additions of trisubstituted acetonide radicals to alkenes. The arrows indicate noncovalent interactions, which dictate the stereoselectivity. (*b*) Correlation plot of experimental and computed diastereoselectivities (using RPA, TPSS, TPSS-D3, and TPSSh-D3) of the reaction of trisubstituted acetonide radicals and methoxybutenolide. The structures were optimized using TPSS-D3/def2-TZVP. Abbreviations: RPA, random-phase approximation; TS, transition state; TPSS, Tao–Perdew–Staroverov–Scuseria; TPSSh, Tao–Perdew–Staroverov–Scuseria hybrid; TZVP, triple-zeta valence plus polarization. Figure adapted from Reference 133 with permission. Copyright 2016 John Wiley and Sons, Inc.

of the transition states; instead, it is essential to account for a delicate balance between weak repulsive and attractive interactions within these systems. As shown in **Figure 8**, the experimental diastereoselectivity closely correlates with theoretical predictions using RPA and the dispersion-corrected TPSS-D3 and TPSSh-D3 functionals (134). The correlation worsens considerably in the absence of dispersion corrections, which underlines the importance of noncovalent interactions for diastereoselectivity in large, crowded systems.

Cave and coworkers (135) studied activation energies in Claisen rearrangements using semilocal and hybrid density functionals, MP2, and RPA. Although all methods yielded similar trends in relative reactivity, the RPA results showed the best agreement with the experimental data.

6.4. Molecular Properties of Closed-Shell Molecules and Radicals

Burow et al. (104) investigated the performance of RPA for molecular properties such as equilibrium structures, dipole moments, and vibrational frequencies of closed-shell systems. As shown in **Figure 9**, RPA generally outperforms PBE and MP2; moreover, similar to MP2, RPA is able to describe intermonomer noncovalent interactions. Using KS references is important for obtaining accurate RPA properties; for example, for the equilibrium bond distances of a set of 17 small molecules, RPA with HF references lead to a mean absolute error (MAE) over three times larger than the MAE obtained from RPA calculations with PBE references (104).

To further assess the accuracy of RPA, we report the equilibrium structures of a variety of small radicals calculated within RPA for the first time (see **Table 3**). These molecules were selected because accurate experimental bond lengths were available in the literature. Radicals are usually short-lived and experimentally elusive intermediates, for which single-reference methods are often unsuitable because of spin contamination and instabilities (136–138). However, RPA structures agree well with experiment, with errors comparable to closed-shell species (see

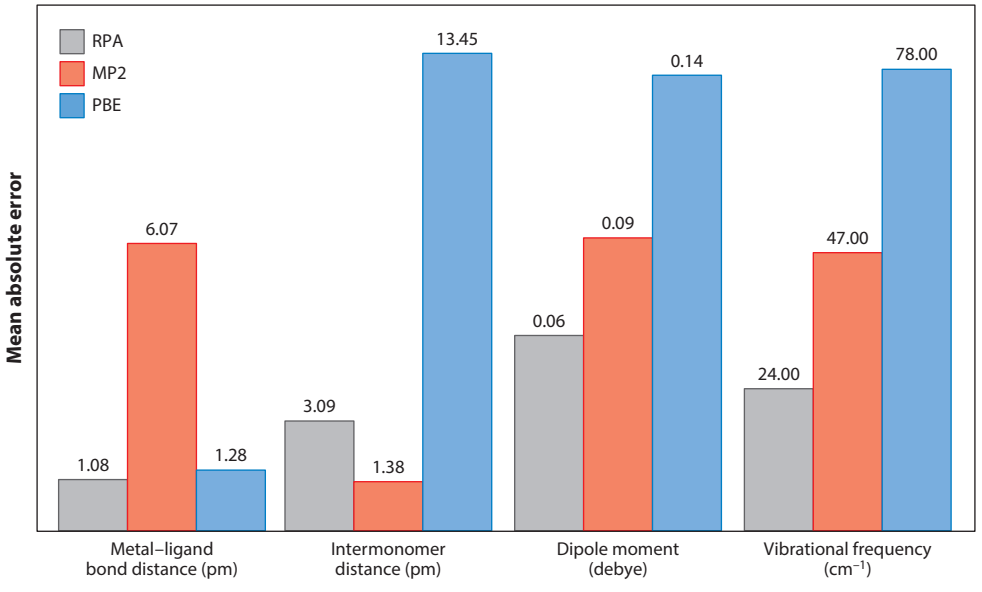

Figure 9

Mean absolute errors of optimized structural properties obtained from RPA, MP2, and PBE. Abbreviations: MP2, second-order Møller–Plesset; PBE, Perdew–Burke–Ernzerhof; RPA, random-phase approximation. Figure adapted from Reference 104 with permission. Copyright 2014 American Chemical Society.

Table 3 Deviations of computed equilibrium bond lengths (in picometers) of small radicals from experimental reference values; MAEs are also provided

	Parameter	Reference value	RPA (TPSS)	RPA (PBE)
OH	O–H	96.97[a]	0.16	0.27
H_2O^+	O–H	100.1[a]	0.02	0.10
HF^+	H–F	100.1[b]	0.40	0.47
NH^+	N–H	107.0[c]	0.28	0.16
HCP^+	H–C	107.3[b]	0.20	0.37
CH_3	C–H	107.67[b]	−0.37	−0.19
N_2^+	N–N	111.642[a]	−0.35	−0.26
CO^+	C–O	112.83[a]	−0.95	−0.82
NO	N–O	115.08[a]	0.42	0.57
CN	C–N	117.18[a]	0.12	0.23
CO_2^+	C–O	117.682[b]	−0.07	0.023
BO	B–O	120.5[a]	0.18	0.31
CF	C–F	127.2[a]	0.44	0.66
F_2^+	F–F	130.5[d]	3.27	3.66
HCP^+	C–P	160.0[b]	−0.39	−0.28
MAE	NA	NA	0.51	0.56

Here, the aug-cc-pV5Z basis set (108) was used. Abbreviations: MAE, mean absolute error; NA, not applicable; PBE, Perdew–Burke–Ernzerhof; RPA, random-phase approximation; TPSS, Tao–Perdew–Staroverov–Scuseria.
[a]Reference 139.
[b]Reference 140.
[c]Reference 141.
[d]Reference 142.

Figure 9). The dependence on the semilocal functional used to generate the KS orbitals is weak, with MAEs of 0.51 pm and 0.56 pm for TPSS and PBE, respectively. The results suggest that RPA is a viable approach for computing structures of open-shell species.

7. CONCLUSIONS

RPA methods encapsulate essential electron correlation effects such as screening, mid- and long-range interactions, and some static correlation even at the level of the bare Coulomb interaction kernel. These effects are largely absent in the description provided by semilocal density functionals, especially for inhomogeneous systems. While semilocal functionals may be empirically adjusted to partially recover the missing effects for certain systems, methods based on RPA offer an appealing alternative that is systematic and widely applicable. Moreover, the sound physical foundation of RPA may guide future method development and provide insight into computational studies, suggesting a possibility to alleviate the functional inflation crisis for both developers and users of DFT.

In computational applications, RPA methods provide a route to assess results from semilocal DFT calculations and even refine them in many cases. These methods are particularly useful for small-gap systems such as metal nanoclusters, *d*- and *f*-element compounds, radicals, and weakly bound complexes, where semilocal DFT results using different functionals typically show wide disparities. Other strengths of RPA methods include the prediction of barrier heights, isogyric

reaction energies, relative energies of conformers, and the description of systems with significant noncovalent interactions. However, processes involving a large change in short-range correlation, such as bond breaking or ionization, require the inclusion of second- and higher-order exchange effects for accurate results. The AXK method efficiently accomplishes this task and greatly reduces self-correlation error in odd-electron systems.

The computational cost of RPA is currently one order of magnitude greater than that of a hybrid DFT calculation. This is already a significant improvement compared to just a few years ago, and with the development of low-scaling algorithms, further reduction of the cost seems possible. RPA methods also require larger basis sets than semilocal DFT for converged results (143). Is this additional cost for an RPA calculation justified? Probably, if the goal of the computational study is to interpret existing results and provide additional evidence for them; certainly, if the goal is to predict the energetics and properties for systems that are difficult or impossible to tackle by other means.

SUMMARY POINTS

1. RPA methods capture screening physics and long-range correlation effects not included in semilocal density functional approximations.
2. RPA methods provide a simple and appealing interpretation of electron correlation in terms of collective charge density fluctuations or plasmonic modes.
3. RPA methods are most accurate for barrier heights, isogyric reaction energies, and systems with significant noncovalent interactions; processes involving bond breaking, spin flipping, or ionization require second- or higher-order exchange to account for short-range correlation effects, e.g., using the AXK approach.
4. The computational cost of an RPA calculation has shrunk to approximately one order of magnitude above that of a semilocal hybrid DFT calculation.
5. RPA methods are particularly useful for small-gap systems such as open-shell d- and f-element compounds and reactive intermediates, where semilocal DFT results exhibit strong functional dependence.

DISCLOSURE STATEMENT

Principal Investigator Filipp Furche has an equity interest in Turbomole GmbH. The terms of this arrangement have been reviewed and approved by the University of California, Irvine, in accordance with its conflict of interest policies.

ACKNOWLEDGMENTS

This material is based upon work supported by the National Science Foundation under CHE-1213382 and CHE-1464828. G.P.C. is grateful to Dr. Mikko Muuronen for helpful discussions.

LITERATURE CITED

1. Pribram-Jones A, Gross DA, Burke K. 2015. DFT: a theory full of holes? *Annu. Rev. Phys. Chem.* 66:283–304

2. Marques MAL, Oliveira MJT, Burnus T. 2012. LIBXC: a library of exchange and correlation functionals for density functional theory. *Comput. Phys. Commun.* 183:2272–81
3. Medvedev MG, Bushmarinov IS, Sun J, Perdew JP, Lyssenko KA. 2017. Density functional theory is straying from the path toward the exact functional. *Science* 355:49–52
4. Mardirossian N, Pestana LR, Womack JC, Skylaris C-K, Head-Gordon T, Head-Gordon M. 2017. Use of the rVV10 nonlocal correlation functional in the B97M-V density functional: defining B97-rV and related functionals. *J. Phys. Chem. Lett.* 8:35–40
5. Furche F, Perdew JP. 2006. The performance of semilocal and hybrid density functionals in 3D transition-metal chemistry. *J. Chem. Phys.* 124:044103
6. Dreuw A, Weisman JL, Head-Gordon M. 2003. Long-range charge-transfer excited states in time-dependent density functional theory require non-local exchange. *J. Chem. Phys.* 119:2943–46
7. Bohm D, Pines D. 1953. A collective description of electron interactions: III. Coulomb interactions in a degenerate electron gas. *Phys. Rev.* 92:609–25
8. Gell-Mann M, Brueckner KA. 1957. Correlation energy of an electron gas at high density. *Phys. Rev.* 106:364–68
9. McLachlan A, Ball M. 1964. Time-dependent Hartree–Fock theory for molecules. *Rev. Mod. Phys.* 36:844–55
10. Oddershede J. 1978. Polarization propagator calculations. *Adv. Quantum Chem.* 11:275–352
11. Szabo A, Ostlund NS. 1977. The correlation energy in the random phase approximation: intermolecular forces between closed-shell systems. *J. Chem. Phys.* 67:4351–60
12. Langreth DC, Perdew JP. 1975. The exchange-correlation energy of a metallic surface. *Solid State Commun.* 17:1425–29
13. Harl J, Kresse G. 2009. Accurate bulk properties from approximate many-body techniques. *Phys. Rev. Lett.* 103:056401
14. Perdew JP, Schmidt K. 2001. Jacob's ladder of density functional approximations for the exchange-correlation energy. *AIP Conf. Proc.* 577:1–20
15. Scuseria GE, Henderson TM, Sorensen DC. 2008. The ground state correlation energy of the random phase approximation from a ring coupled cluster doubles approach. *J. Chem. Phys.* 129:231101
16. Oddershede J. 1987. Propagator methods. In *Advances in Chemical Physics: Ab Initio Methods in Quantum Chemistry II*, ed. KP Lawley, pp. 201–39. New York: Wiley
17. Onida G, Reining L, Rubio A. 2002. Electronic excitations: density-functional versus many-body Green's-function approaches. *Rev. Mod. Phys.* 74:601–59
18. Dobson JF. 2012. Dispersion (van der Waals) forces and TDDFT. In *Fundamentals of Time-Dependent Density Functional Theory*, ed. MAL Marques, NT Maitra, FMS Nogueira, EKU Gross, A Rubio, pp. 417–41. Berlin: Springer
19. Heßelmann A, Görling A. 2011. Random-phase approximation correlation methods for molecules and solids. *Mol. Phys.* 109:2473–500
20. Eshuis H, Bates JE, Furche F. 2012. Electron correlation methods based on the random phase approximation. *Theor. Chem. Acc.* 131:1084
21. Ren X, Rinke P, Joas C, Scheffler M. 2012. Random-phase approximation and its applications in computational chemistry and materials science. *J. Mater. Sci.* 47:7447–71
22. Dobson JF, Gould T. 2012. Calculation of dispersion energies. *J. Phys. Condens. Matter* 24:073201
23. Scuseria GE, Henderson TM, Bulik IW. 2013. Particle-particle and quasiparticle random phase approximations: connections to coupled cluster theory. *J. Chem. Phys.* 139:104113
24. Shepherd JJ, Henderson TM, Scuseria GE. 2014. Coupled cluster channels in the homogeneous electron gas. *J. Chem. Phys.* 140:124102
25. van Aggelen H, Yang Y, Yang W. 2014. Exchange-correlation energy from pairing matrix fluctuation and the particle–particle random phase approximation. *J. Chem. Phys.* 140:18A511
26. Shenvi N, van Aggelen H, Yang Y, Yang W. 2014. Tensor hypercontracted ppRPA: reducing the cost of the particle–particle random phase approximation from $O(r^6)$ to $O(r^4)$. *J. Chem. Phys.* 141:024119
27. Janesko BG, Henderson TM, Scuseria GE. 2009. Long-range-corrected hybrid density functionals including random phase approximation correlation: application to noncovalent interactions. *J. Chem. Phys.* 131:034110

28. Mussard B, Reinhardt P, Ángyán JG, Toulouse J. 2015. Spin-unrestricted random-phase approximation with range separation: benchmark on atomization energies and reaction barrier heights. *J. Chem. Phys.* 142:154123
29. Mezei PD, Csonka GI, Ruzsinszky A, Kallay M. 2015. Construction and application of a new dual-hybrid random phase approximation. *J. Chem. Theory Comput.* 11:4615–26
30. Grimme S, Steinmetz M. 2016. A computationally efficient double hybrid density functional based on the random phase approximation. *Phys. Chem. Chem. Phys.* 18:20926–37
31. Kats D, Manby FR. 2013. The distinguishable cluster approximation. *J. Chem. Phys.* 139:021102
32. Shepherd JJ, Henderson TM, Scuseria GE. 2014. Range-separated Brueckner coupled cluster doubles theory. *Phys. Rev. Lett.* 112:133002
33. Tkatchenko A, DiStasio RAJ, Car R, Scheffler M. 2012. Accurate and efficient method for many-body van der Waals interactions. *Phys. Rev. Lett.* 108:236402
34. Odbadrakh TT, Voora V, Jordan KD. 2015. Application of electronic structure methods to coupled Drude oscillators. *Chem. Phys. Lett.* 630:76–79
35. Kohn W, Sham LJ. 1965. Self-consistent equations including exchange and correlation effects. *Phys. Rev.* 140:A1133–38
36. Gunnarsson O, Lundqvist BI. 1976. Exchange and correlation in atoms, molecules, and solids by spin-density functional formalism. *Phys. Rev. B* 13:4274–98
37. Hohenberg P, Kohn W. 1964. Inhomogeneous electron gas. *Phys. Rev.* 136:B864–71
38. Görling A, Levy M. 1993. Correlation-energy functional and its high-density limit obtained from a coupling-constant perturbation expansion. *Phys. Rev. B* 47:13105–13
39. Callen HB, Welton TA. 1951. Irreversibility and generalized noise. *Phys. Rev.* 83:34–40
40. Langreth D, Perdew J. 1977. Exchange-correlation energy of a metallic surface: wave-vector analysis. *Phys. Rev. B* 15:2884–901
41. Runge E, Gross EKU. 1984. Density-functional theory for time-dependent systems. *Phys. Rev. Lett.* 52:997–1000
42. Ullrich CA. 2011. *Time-Dependent Density-Functional Theory: Concepts and Applications*. Oxford, UK: Oxford Univ. Press
43. Linderberg J, Öhrn Y. 1973. *Propagators in Quantum Chemistry*. London: Academic
44. Casida ME. 1995. Time-dependent density functional response theory for molecules. In *Recent Advances in Density Functional Methods*, Part I, ed. DA Chong, pp. 155–92. Singapore: World Sci.
45. Bauernschmitt R, Ahlrichs R. 1996. Treatment of electronic excitations within the adiabatic approximation of time dependent density functional theory. *Chem. Phys. Lett.* 256:454–64
46. Furche F. 2001. On the density matrix based approach to time-dependent density functional response theory. *J. Chem. Phys.* 114:5982–92
47. Fetter AL, Walecka JD. 1971. *Quantum Theory of Many-Particle Systems*. New York: McGraw-Hill
48. Petersilka M, Gossmann U, Gross E. 1996. Excitation energies from time-dependent density-functional theory. *Phys. Rev. Lett.* 76:1212–15
49. Pines D. 1963. *Elementary Excitations in Solids*. New York: Benjamin
50. Dobson JF, Wang J, Dinte BP, McLennan K, Le HM. 2005. Soft cohesive forces. *Int. J. Quantum Chem.* 101:579–98
51. Jeziorski B, Moszynski R, Szalewicz K. 1994. Perturbation theory approach to intermolecular potential energy surfaces of van der Waals complexes. *Chem. Rev.* 94:1887–930
52. Heßelmann A, Jansen G. 2002. Intermolecular induction and exchange-induction energies from coupled-perturbed Kohn–Sham density functional theory. *Chem. Phys. Lett.* 362:319–25
53. Misquitta AJ, Szalewicz K. 2005. Symmetry-adapted perturbation-theory calculations of intermolecular forces employing density-functional description of monomers. *J. Chem. Phys.* 122:214109
54. Furche F. 2008. Developing the random phase approximation into a practical post-Kohn–Sham correlation model. *J. Chem. Phys.* 129:114105
55. Krauter CM, Bernadotte S, Jacob CR, Pernpointner M, Dreuw A. 2015. Identification of plasmons in molecules with scaled ab initio approaches. *J. Phys. Chem. C* 119:24564–73
56. Furche F. 2001. Molecular tests of the random phase approximation to the exchange-correlation energy functional. *Phys. Rev. B* 64:195120

57. Wang J, Wang G, Zhao J. 2003. Structures and electronic properties of Cu_{20} , Ag_{20} , and Au_{20} clusters with density functional method. *Chem. Phys. Lett.* 380:716–20
58. Weigend F, Ahlrichs R. 2005. Balanced basis sets of split valence, triple zeta valence and quadruple zeta valence quality for H to Rn: design and assessment of accuracy. *Phys. Chem. Chem. Phys.* 7:3297–305
59. Andrae D, Häußermann U, Dolg M, Stoll H, Preuß H. 1990. Energy-adjusted ab initio pseudopotentials for the second and third row transition elements. *Theor. Chim. Acta* 77:123–41
60. Tao J, Perdew J, Staroverov V, Scuseria GE. 2003. Climbing the density functional ladder: nonempirical meta-generalized gradient approximation designed for molecules and solids. *Phys. Rev. Lett.* 91:146401
61. Treutler O, Ahlrichs R. 1995. Efficient molecular numerical integration schemes. *J. Chem. Phys.* 102:346–54
62. Sottile F, Olevano V, Reining L. 2003. Parameter-free calculation of response functions in time-dependent density-functional theory. *Phys. Rev. Lett.* 91:056402
63. Salpeter EE, Bethe HA. 1951. A relativistic equation for bound-state problems. *Phys. Rev.* 84:1232–42
64. Feynman RP. 1949. Space-time approach to quantum electrodynamics. *Phys. Rev.* 76:769–89
65. Dyson FJ. 1949. The radiation theories of Tomonaga, Schwinger, and Feynman. *Phys. Rev.* 75:486–502
66. Goldstone J. 1957. Derivation of the Brueckner many-body theory. *Proc. R. Soc. A* 239:267–79
67. Singwi K, Tosi M, Land R, Sjölander A. 1968. Electron correlations at metallic densities. *Phys. Rev.* 176:589–99
68. Bates JE, Furche F. 2013. Random phase approximation renormalized many-body perturbation theory. *J Chem. Phys.* 139:171103
69. Grüneis A, Marsman M, Harl J, Schimka L, Kresse G. 2009. Making the random phase approximation to electronic correlation accurate. *J. Chem. Phys.* 131:154115
70. Freeman DL. 1977. Coupled-cluster expansion applied to the electron gas: inclusion of ring and exchange effects. *Phys. Rev. B* 15:5512–21
71. Ángyán JG, Liu RF, Toulouse J, Jansen G. 2011. Correlation energy expressions from the adiabatic-connection fluctuation–dissipation theorem approach. *J. Chem. Theory Comput.* 7:3116–30
72. Paier J, Janesko BG, Henderson TM, Scuseria GE, Grüneis A, Kresse G. 2010. Hybrid functionals including random phase approximation correlation and second-order screened exchange. *J. Chem. Phys.* 132:094103
73. Shavitt I, Bartlett RJ. 2009. *Many-Body Methods in Chemistry and Physics: MBPT and Coupled-Cluster Theory*. Cambridge, UK: Cambridge Univ. Press
74. Talman J, Shadwick W. 1976. Optimized effective atomic central potential. *Phys. Rev. A* 14:36–40
75. Bleiziffer P, Heßelmann A, Görling A. 2012. Resolution of identity approach for the Kohn–Sham correlation energy within the exact-exchange random-phase approximation. *J. Chem. Phys.* 136:134102
76. Görling A, Levy M. 1994. Exact Kohn–Sham scheme based on perturbation theory. *Phys. Rev. A* 50:196–204
77. Hellgren M, von Barth U. 2007. Correlation potential in density functional theory at the GWA level: spherical atoms. *Phys. Rev. B* 76:075107
78. Hellgren M, Rohr DR, Gross EKU. 2012. Correlation potentials for molecular bond dissociation within the self-consistent random phase approximation. *J. Chem. Phys.* 136:034106
79. Verma P, Bartlett RJ. 2012. Increasing the applicability of density functional theory. II. Correlation potentials from the random phase approximation and beyond. *J. Chem. Phys.* 136:044105
80. Bleiziffer P, Krug M, Görling A. 2015. Self-consistent Kohn–Sham method based on the adiabatic-connection fluctuation-dissipation theorem and the exact-exchange kernel. *J. Chem. Phys.* 142:244108
81. Hirata S, Ivanov S, Grabowski I, Bartlett RJ. 2002. Time-dependent density functional theory employing optimized effective potentials. *J. Chem. Phys.* 116:6468–81
82. Shigeta Y, Hirao K, Hirata S. 2006. Exact-exchange time-dependent density-functional theory with the frequency-dependent kernel. *Phys. Rev. A* 73:010502
83. Staroverov VN, Scuseria GE, Davidson ER. 2006. Optimized effective potentials yielding Hartree–Fock energies and densities. *J. Chem. Phys.* 124:141103
84. Heßelmann A, Ipatov A, Görling A. 2009. Charge-transfer excitation energies with a time-dependent density-functional method suitable for orbital-dependent exchange-correlation kernels. *Phys. Rev. A* 80:012507

85. Ryabinkin IG, Kohut SV, Staroverov VN. 2015. Reduction of electronic wave functions to Kohn–Sham effective potentials. *Phys. Rev. Lett.* 115:083001
86. Weigend F, Häser M. 1997. RI-MP2: first derivatives and global consistency. *Theor. Chim. Acta* 97:331–40
87. Dunlap BI, Conolly JWD, Sabin JR. 1979. Some approximations in applications of X-alpha theory. *J. Chem. Phys.* 71:3396–402
88. Weigend F, Köhn A, Hättig C. 2002. Efficient use of the correlation consistent basis sets in resolution of the identity MP2 calculations. *J. Chem. Phys.* 116:3175–83
89. Eshuis H, Yarkony J, Furche F. 2010. Fast computation of molecular random phase approximation correlation energies using resolution of the identity and imaginary frequency integration. *J. Chem. Phys.* 132:234114
90. Heßelmann A. 2012. Random-phase-approximation correlation method including exchange interactions. *Phys. Rev. A* 85:012517
91. Boyd JP. 1987. Exponentially convergent Fourier–Chebshev quadrature schemes on bounded and infinite intervals. *J. Sci. Comput.* 2:99–109
92. Kaltak M, Klimeš J, Kresse G. 2014. Low scaling algorithms for the random phase approximation: imaginary time and Laplace transformations. *J. Chem. Theory Comput.* 10:2498–507
93. Schurkus HF, Ochsenfeld C. 2016. An effective linear-scaling atomic-orbital reformulation of the random-phase approximation using a contracted double-Laplace transformation. *J. Chem. Phys.* 144:031101
94. Moussa JE. 2014. Cubic-scaling algorithm and self-consistent field for the random-phase approximation with second-order screened exchange. *J. Chem. Phys.* 140:014107
95. Baerends EJ, Ellis DE, Ros P. 1973. Self-consistent molecular Hartree–Fock–Slater calculations I. The computational procedure. *Chem. Phys.* 2:41–51
96. Hohenstein EG, Parrish RM, Martínez TJ. 2012. Tensor hypercontraction density fitting. I. Quartic scaling second- and third-order Møller–Plesset perturbation theory. *J. Chem. Phys.* 137:044103
97. Kallay M. 2015. Linear-scaling implementation of the direct random-phase approximation. *J. Chem. Phys.* 142:204105
98. Risthaus T, Grimme S. 2013. Benchmarking of London dispersion-accounting density functional theory methods on very large molecular complexes. *J. Chem. Theory Comput.* 9:1580–91
99. Perdew JP, Burke K, Ernzerhof M. 1996. Generalized gradient approximation made simple. *Phys. Rev. Lett.* 77:3865–68. Erratum. *Phys. Rev. Lett.* 78:1396
100. Perdew JP, Burke K, Ernzerhof M. 1998. Perdew, Burke, and Ernzerhof reply. *Phys. Rev. Lett.* 80:891
101. Pulay P. 2007. Analytical derivative methods in quantum chemistry. *Adv. Chem. Phys.* 69:241–86
102. Helgaker T, Jørgensen P, Handy NC. 1989. A numerically stable procedure for calculating Møller–Plesset energy derivatives, derived using the theory of Lagrangians. *Theor. Chim. Acta* 76:227–45
103. Jørgensen P, Helgaker T. 1988. Møller–Plesset energy derivatives. *J. Chem. Phys.* 89:1560–70
104. Burow AM, Bates JE, Furche F, Eshuis H. 2014. Analytical first-order molecular properties and forces within the adiabatic connection random phase approximation. *J. Chem. Theory Comput.* 10:180–94
105. Pople JA, Krishnan R, Schlegel HB, Binkley JS. 1979. Derivative studies in Hartree–Fock and Møller–Plesset theories. *Int. J. Quantum Chem.* 16:225–41
106. Fuchs M, Niquet YM, Gonze X, Burke K. 2005. Describing static correlation in bond dissociation by Kohn–Sham density functional theory. *J. Chem. Phys.* 122:094116
107. Henderson TM, Scuseria GE. 2010. The connection between self-interaction and static correlation: a random phase approximation perspective. *Mol. Phys.* 108:2511–17
108. Woon DE, Dunning TH Jr. 1994. Gaussian basis sets for use in correlated molecular calculations. IV. Calculation of static electrical response properties. *J. Chem. Phys.* 100:2975–88
109. Deglmann P, Furche F, Ahlrichs R. 2002. An efficient implementation of second analytical derivatives for density functional methods. *Chem. Phys. Lett.* 362:511–18
110. Furche F, Krull BT, Nguyen BD, Kwon J. 2016. Accelerating molecular property calculations with nonorthonormal Krylov space methods. *J. Chem. Phys.* 144:174105
111. Rekkedal J, Coriani S, Iozzi MF, Teale AM, Helgaker T, Pedersen TB. 2013. Analytic gradients in the random-phase approximation. *J. Chem. Phys.* 139:081101

112. Mussard B, Szalay PG, Ángyán JG. 2014. Analytical energy gradients in range-separated hybrid density functional theory with random phase approximation. *J. Chem. Theory. Comput.* 10:1968–79
113. Hammer B, Norskov JK. 1995. Why gold is the noblest of all the metals. *Nature* 376:238–40
114. Haruta M, Daté M. 2001. Advances in the catalysis of Au nanoparticles. *Appl. Catal. A* 222:427–37
115. Liu X, He L, Liu YM, Cao Y. 2014. Supported gold catalysis: from small molecule activation to green chemical synthesis. *Acc. Chem. Res.* 47:793–804
116. Zhang C, Yoon B, Landman U. 2007. Predicted oxidation of Co catalyzed by Au nanoclusters on a thin defect-free MgO film supported on a Mo(100) surface. *J. Am. Chem. Soc.* 129:2228–29
117. Gilb S, Weis P, Furche F, Ahlrichs R, Kappes MM. 2002. Structures of small gold cluster cations (Au_n^+, $n < 14$): ion mobility measurements versus density functional calculations. *J. Chem. Phys.* 116:4094–101
118. Johansson MP, Lechtken A, Schooss D, Kappes MM, Furche F. 2008. 2D–3D transition transition of gold cluster anions resolved. *Phys. Rev. A* 77:053202
118a. Gruene P, Rayner DM, Redlich B, van der Meer AFG, Lyon JT, et al. 2008. Structures of neutral Au_7, Au_{19}, and Au_{20} clusters in the gas phase. *Science* 321:674–76
119. Gruene P, Butschke B, Lyon JT, Rayner DM, Fielicke A. 2014. Far-IR spectra of small neutral gold clusters in the gas phase. *Z. Phys. Chem.* 228:337–50
119a. Wang J, Wang G, Zhao J. 2002. Density-functional study of Au_n ($n = 2$–20) clusters: lowest-energy structures and electronic properties. *Phys. Rev. B* 66:035418
120. Dong Y, Springborg M. 2007. Global structure optimization study on $Au_{2–20}$. *Eur. Phys. J. D* 43:15–18
121. Assadollahzadeh B, Schwerdtfeger P. 2009. A systematic search for minimum structures of small gold clusters Au_n ($n = 2$–20) and their electronic properties. *J. Chem. Phys.* 131:064306
122. Hansen JA, Piecuch P, Levine BG. 2013. Determining the lowest-energy isomer of Au_8: 2D, or not 2D. *J. Chem. Phys.* 139:091101
123. Johnston RL. 2003. Evolving better nanoparticles: genetic algorithms for optimising cluster geometries. *Dalton Trans.* 2003:4193–207
124. Johansson MP, Warnke I, Le A, Furche F. 2014. At what size do neutral gold clusters turn three-dimensional? *J. Phys. Chem. C* 118:29370–77
125. Perdew JP, Ruzsinszky A, Csonka GI, Constantin LA, Sun J. 2009. Workhorse semilocal density functional for condensed matter physics and quantum chemistry. *Phys. Rev. Lett.* 103:026403
126. Fernández EM, Soler JM, Garzón IL, Balbás LC. 2004. Trends in the structure and bonding of noble metal clusters. *Phys. Rev. B* 70:165403
127. Fieser ME, Mueller TJ, Bates JE, Ziller JW, Furche F, Evans WJ. 2014. Differentiating chemically similar Lewis acid sites in heterobimetallic complexes: the rare-earth bridged hydride $(C_5Me_5)_2Ln(\mu\text{-}H)_2Ln'(C_5Me_5)_2$ and tuckover hydride $(C_5Me_5)_2Ln(\mu\text{-}H)(\mu\text{-}\eta^1{:}\eta^5\text{-}CH_2C_5Me_4)\text{-}Ln'(C_5Me_5)$ systems. *Organometallics* 33:3882–90
128. Grimme S, Antony J, Ehrlich S, Krieg H. 2010. A consistent and accurate ab initio parametrization of density functional dispersion correction (DFT-D) for the 94 elements H–Pu. *J. Comput. Chem.* 132:154104
129. MacDonald MR, Fieser ME, Bates JE, Ziller JW, Furche F, Evans WJ. 2013. Identification of the +2 oxidation state for uranium in a crystalline molecular complex, [K(2.2.2-cryptand)][$(C_5H_4SiMe_3)_3U$]. *J. Am. Chem. Soc.* 135:13310–13
130. Bates JE. 2013. *First principles studies of heavy-metal chemistry and RPA-renormalized perturbation theory*. Ph.D. Thesis, Univ. Calif., Irvine
131. Becke AD. 1993. Density-functional thermochemistry. III. The role of exact exchange. *J. Chem. Phys.* 98:5648–52
132. Lee C, Yang W, Parr RG. 1988. Development of the Colle–Salvetti correlation-energy formula into a functional of the electron density. *Phys. Rev. B* 37:785–89
133. Tao DJ, Muuronen M, Slutskyy Y, Le A, Furche F, Overman LE. 2016. Diastereoselective coupling of chiral acetonide trisubstituted radicals with alkenes. *Chem. Eur. J.* 22:8786–90
133a. Tao DJ, Slutskyy Y, Overman LE. Total synthesis of (–)-chromodorolide B. *J. Am. Chem. Soc.* 138:2186–89
134. Staroverov VN, Scuseria GE. 2003. Comparative assessment of a new nonempirical density functional: molecules and hydrogen-bonded complexes. *J. Chem. Phys.* 119:12129–37

135. Hartley MK, Vine S, Walsh E, Avrantinis S, Daub GW, Cave RJ. 2016. Comparison of relative activation energies obtained by density functional theory and the random phase approximation for several Claisen rearrangements. *J. Phys. Chem. B* 120:1486–96
136. Fukutome H. 1981. Unrestricted Hartree–Fock theory and its applications to molecules and chemical reactions. *Int. J. Quantum Chem.* 20:955–1065
137. Thouless DJ. 2013. *The Quantum Mechanics of Many-Body Systems*. Mineola, NY: Dover
138. Stanton JF, Gauss J. 2003. A discussion of some problems associated with the quantum mechanical treatment of open-shell molecules. *Adv. Chem. Phys.* 125:101–46
139. Huber KP, Herzberg G. 2013. *Molecular Spectra and Molecular Structure: IV. Constants of Diatomic Molecules*. New York: Springer
140. Graner G, Kuchitsu K. 2001. *Structure Data of Free Polyatomic Molecules. Landolt–Börnstein: Molecules and Radicals*. Berlin: Springer
141. Harmony MD, Laurie VW, Kuczkowski RL, Schwendeman RH, Ramsay DA, et al. 1979. Molecular structures of gas-phase polyatomic molecules determined by spectroscopic methods. *J. Phys. Chem. Ref. Data* 8:619–722
142. Tuckett RP, Dale AR, Jaffey DM, Jarrett PS, Kelly T. 1983. The $\tilde{A}\,^2\Pi_u \rightarrow \tilde{X}\,^2\Pi_g$ electronic emission spectrum of the fluorine molecular ion $F_2{}^+$ studied in a supersonic beam. *Mol. Phys.* 49:475–86
143. Eshuis H, Furche F. 2012. Basis set convergence of molecular correlation energy differences within the random phase approximation. *J. Chem. Phys.* 136:084105

Annual Review of
Physical Chemistry
Volume 68, 2017

Contents

Indexes

Errata

An online log of corrections to *Annual Review of Physical Chemistry* articles may be found at http://www.annualreviews.org/errata/physchem